

Instance Segmentation of Unlabeled Modalities via Cyclic Segmentation GAN

Leander Lauenburg^{1,2*}, Zudi Lin^{1*†}, Ruihan Zhang³, Márcia dos Santos⁴, Siyu Huang¹, Ignacio Arganda-Carreras^{5,6,7}, Edward S. Boyden^{3,8}, Hanspeter Pfister¹, and Donglai Wei⁹

¹Harvard University ²Technical University of Munich ³MIT ⁴University of Cambridge ⁵Donostia International Physics Center ⁶University of the Basque Country ⁷Ikerbasque, Basque Foundation for Science ⁸HHMI ⁹Boston College

Abstract. Instance segmentation for unlabeled imaging modalities is a challenging but essential task as collecting expert annotation can be expensive and time-consuming. Existing works segment a new modality by either deploying a pre-trained model optimized on diverse training data or conducting domain translation and image segmentation as two independent steps. In this work, we propose a novel *Cyclic Segmentation* Generative Adversarial Network (**CySGAN**) that conducts image translation and instance segmentation jointly using a unified framework. Besides the CycleGAN losses for image translation and supervised losses for the annotated source domain, we introduce additional self-supervised and segmentation-based adversarial objectives to improve the model performance by leveraging unlabeled target domain images. We benchmark our approach on the task of 3D *neuronal nuclei* segmentation with annotated electron microscopy (EM) images and unlabeled expansion microscopy (ExM) data. Our CySGAN outperforms both pre-trained generalist models and the baselines that sequentially conduct image translation and segmentation. Our implementation and the newly collected, densely annotated ExM nuclei dataset, named *NucExM*, are available at <https://connectomics-bazaar.github.io/proj/CySGAN/index.html>.

Keywords: 3D Instance Segmentation · Unsupervised Domain Adaptation · Expansion Microscopy (ExM) · Electron Microscopy (EM)

1 Introduction

3D Instance segmentation of cell nuclei is an essential topic attracting both biomedical and computer vision researchers [21,1,24,27,16]. Supervised deep learning with in-domain annotations (*e.g.*, U-Net [22,4]) has become the dominant methodology for common imaging modalities. However, for novel imaging techniques, *e.g.*, expansion microscopy (ExM) [3], such an approach is less applicable to newly collected large-scale data due to the high annotation cost.

* These authors contributed equally to this work.

† Corresponding author. Email: linzudi@g.harvard.edu

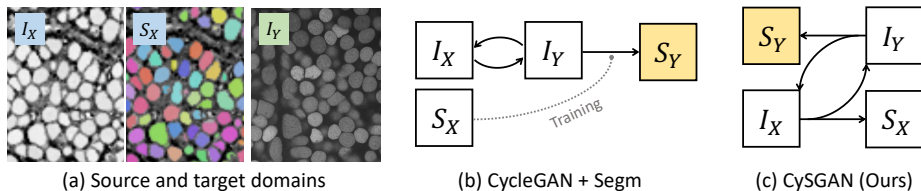


Fig. 1: Overview of task and methods. **(a)** We aim to segment an unlabeled target domain (I_Y) by leveraging the images (I_X) and masks (S_X) in the source domain. Instead of **(b)** conducting image translation (*e.g.*, via CycleGAN [28]) and instance segmentation as two separate steps, we propose **(c)** the CySGAN framework to unify the two functionalities, optimized with both image translation as well as supervised and *semi-supervised* segmentation losses.

To address the challenges, two common approaches aim to make use of existing labels for the unlabeled domain. One approach is to train a supervised model on diverse datasets and then directly apply it to the new domain [24,27]. However, they can hardly be adapted to a new domain without label images. The other way makes use of unpaired image-to-image translation models like CycleGAN [28]. First, source images are translated to match the target domain distribution, aiming to be indistinguishable from the target domain while keeping the source structures. Next, the masks and translated images are used to train a supervised model and segment target images¹ (Fig. 1b). However, the segmentation depends on a translation model optimized regardless of the downstream task, while two separate modules also increase the pipeline complexity.

In this work, we propose a *Cyclic Segmentation* Generative Adversarial Network (CySGAN) that unifies image translation and segmentation to tackle unlabeled modalities (Fig. 1c). For both the source and target domains, we train a single 3D U-Net [4] that takes only images as input but outputs both segmentation and translated images simultaneously. Besides optimizing the translation and supervised segmentation losses as previous work [17], we introduce structural consistency and segmentation-based adversarial losses to better leverage the unlabeled domain images, connecting ideas from *semi-supervised* segmentation. Moreover, to incorporate data augmentations shown to enhance segmentation performance [13,16], we enforce the cycle consistency [28] of the reconstructed images to the clean images instead of the augmented ones, which acts as regularization and enable the model to restore corrupted regions.

In addition, we curated and annotated two expansion microscopy (ExM) image volumes from an adult zebrafish brain tissue with dense cell nuclei (I_Y in Fig. 1a). These two volumes are complemented by a publicly available and labeled electron microscopy (EM) dataset (I_X and S_X in Fig. 1a). Without any

¹ The opposite way, which transfers the target images to the source domain and applies a supervised model trained on the source, is also reasonable. However, it is used less often as both the translation and segmentation models are required in inference.

annotation for the ExM domain, our CySGAN outperforms models pretrained on diverse datasets and the methods that conduct translation and segmentation separately. We release our code and the new *NucExM* dataset for future research.

1.1 Related Works

Unpaired Image-to-Image Translation. Paired images from different domains are expensive or even infeasible to obtain. Therefore, *unpaired* image-to-image translation [11,28] based on Generative Adversarial Networks (GAN) [8] becomes a sensible methodology to transfer source images to the target distribution. CycleGAN [28] achieves impressive performance by ensuring *cycle consistency* when transferring translated images back to the input domain. Further improvements including shared high-level layers [18] and latent space alignment [9]. We refer readers to the survey by Pang *et al.* [20] for a more detailed discussion on image-to-image translation. In particular, our work focus on combining image translation with segmentation models to tackle unlabeled modalities.

Instance Segmentation of 3D Microscopy. 3D instance segmentation from microscopy images is challenging due to the dense distribution of objects and unavoidable physical limitations in imaging (*e.g.*, data is frequently anisotropic). Recent learning-based approaches tackle these challenges by first optimizing CNN-based models to predict representations calculated from the instance masks, including object boundary [5,22,26], affinity map [25,13], star-convex distance [27], flow-field [24] and the combination of multiple representations [16]. Watershed transform [7,29] and graph partition [12] can then be applied to convert the predicted representations into instance masks. However, most existing works train the segmentation models in a supervised learning manner, which becomes infeasible considering the cost of acquiring expert annotations for new modalities. Our work focuses on unifying segmentation approaches with image translation to segment instances in new domains via unsupervised domain adaptation.

Combining Translation and Segmentation. Segmenting unlabeled domains via image translation is a practical methodology. Chartsias *et al.* [2] design a two-stage framework that first translates label images to the unlabeled domain using CycleGAN [28], then trains a separate segmentation model using the synthesized images and original ground-truth label. CyCADA [9] and EssNet [10] improve the sequential model by jointly optimizing the translation and segmentation networks. However, using two separate models increases the system complexity in training and deployment. The concept to simultaneously conduct translation and segmentation has been explored in SUSAN [17], but our work differs from it in two main aspects. First, SUSAN is for 2D semantic segmentation, while our work focuses on the more challenging 3D instance segmentation. Second, SUSAN only applies supervised segmentation losses to the annotated domain, while our CySGAN leverages structural consistency and segmentation-based adversarial losses for the unlabeled domain in the absence of ground-truth labels.

2 Method

Suppose we have an annotated *source* domain $X = (I_X, S_X)$ where I_X and S_X denote the images and paired segmentation labels, respectively. Then for an unlabeled *target* domain Y with only I_Y , the goal is to generate the instance segmentation S_Y without any manual annotations in the Y domain. An idea is to first synthesize images $I_{Y'} = F(I_X)$ that are *indistinguishable* from the distribution of I_Y but keep the instance structure in S_X . Then a supervised model can be optimized using $(I_{Y'}, S_X)$ pairs to predict S_Y from I_Y (Fig. 1b).

Although it is straightforward to conduct translation and segmentation *sequentially*, the translation model is not designed with an end task in mind and can propagate errors to the second step. Besides, the two separate modules make the system complicated in training and deployment. Thus, we propose a framework to finish translation and instance segmentation *simultaneously* using two generators that output both translated images and segmentation (Fig. 1c):

$$F : I_X \rightarrow (I_Y, S_X) \quad B : I_Y \rightarrow (I_X, S_Y) \quad (1)$$

We denote the proposed framework as the *cyclic segmentation GAN* (CySGAN). Specifically, for an image $x_i \sim I_X$, we have $[\hat{y}_i, \hat{x}_s] = F(x_i)$, where \hat{y}_i is the synthesized image, \hat{x}_s contains the predicted instance representations (will elaborate later), and $[\hat{y}_i, \hat{x}_s]$ is their concatenation (a single model outputs them as different channels). For clarity in formulations, we also denote $\hat{y}_i = F(x_i)_{[I]}$ and $\hat{x}_s = F(x_i)_{[S]}$. Note that $B(F(x_i))$ is no longer a valid expression as both models take only an image as input but output the translated image and segmentation.

We optimize F and B together with the necessary discriminators and segment I_Y with B . Our design largely simplifies the sequential framework with two isolated steps. Different from standard image translation, the two domains are *asymmetric*, as X is labeled, while Y is unlabeled. We thus apply similar image translation losses but unique segmentation losses for X and Y domains.

2.1 Image Translation Losses

We denote F as the *forward* generator. Since paired I_X and I_Y are difficult or even infeasible to obtain, F is usually optimized using the *adversarial* loss:

$$\mathcal{L}_{GAN}(F, D_Y^I) = \log D_Y^I(y_i) + \log(1 - D_Y^I(\hat{y}_i)), \quad \hat{y}_i = F(x_i)_{[I]} \quad (2)$$

where D_Y^I is the I_Y discriminator, while y_i and \hat{y}_i are true and synthesized images, respectively. Following CycleGAN [28], we also use the *backward* generator B and an I_X discriminator D_X^I to symmetrically optimize $\mathcal{L}_{GAN}(B, D_X^I)$, as well as enforcing the *cycle-consistency* loss for the images in both domains:

$$\mathcal{L}_{cyc}(F, B) = \|B(\hat{y}_i)_{[I]} - x_i\|_1 + \|F(\hat{x}_i)_{[I]} - y_i\|_1 \quad (3)$$

The losses enable the models to transfer images between I_X and I_Y distributions.

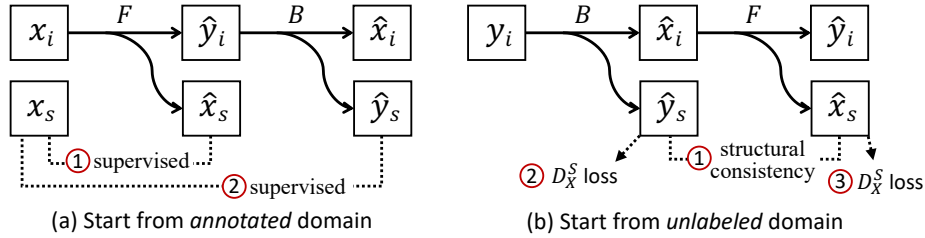


Fig. 2: Segmentation losses. **(a)** For an annotated image in X , we compute the supervised losses of predicted representations against the label. **(b)** For an unlabeled image in Y , we enforce *structural consistency* between predicted representations (as the underlying structures should be shared) and also adversarial losses to improve the quality of predictions in the absence of paired labels.

2.2 Instance Segmentation Losses

Labeled Source Domain. Instance segmentation approaches for microscopy images [24,27,26,16] usually predict instance representations computed from the permutation-invariant labels and then apply a decoding algorithm to yield the masks. In this work, we follow U3D-BCD [16] that predicts the *binary foreground mask* (B), *instance contour map* (C), and *signed distance transform* (D) as three output channels using a 3D U-Net [4], which are decoded by a marker-controlled watershed (MW) algorithm. The B and C channels are optimized with the binary cross-entropy loss (BCE), while D is regressed with the mean squared error (MSE). Given an image-label pair (x_i, x_s) sampled from (I_X, S_X) , the loss is

$$\mathcal{L}_{seg}(F) = \mathcal{L}_{bce}\left(F(x_i)_{[S]}^B, x_s^B\right) + \mathcal{L}_{bce}\left(F(x_i)_{[S]}^C, x_s^C\right) + \|F(x_i)_{[S]}^D - x_s^D\|_2^2 \quad (4)$$

where $x_s = [x_s^B, x_s^C, x_s^D]$ is the concatenation of the three representations. $\mathcal{L}_{seg}(F)$ and another segmentation loss $\mathcal{L}_{seg}(B)$ (based on the synthesized \hat{y}_i) are optimized by directly comparing \hat{x}_s and \hat{y}_s with x_s from S_X (① and ② in Fig. 2a).

The loss $\mathcal{L}_{seg}(B)$ effectively trains B in a supervised manner to predict the segmentation representations. Moreover, this design is not restricted to a particular representation and can be easily modified to incorporate other approaches.

Unlabeled Target Domain. Since Y is unlabeled, it is impossible to apply the supervised losses for X . To further improve segmentation quality, we introduce a *structural consistency* loss between the segmentation outputs of both generators, \hat{y}_s and \hat{x}_s (① Fig. 2b), as they should share identical underlying structures even if the inputs are from two modalities. This loss $\mathcal{L}_{sc}(F, B)$ is formulated as

$$\mathcal{L}_{sc}(F, B) = \|B(y_i)_{[S]} - F(B(y_i)_{[I]})_{[S]}\|_1 \quad (5)$$

We also add structure-based adversarial losses (② and ③ in Fig. 2b) to the predictions to enforce their distributional similarity with S_X (called $\mathcal{L}_{GAN}(B, D_X^S)$ and $\mathcal{L}_{GAN}(F, D_X^S)$). Specifically, the discriminator D_X^S takes the concatenation

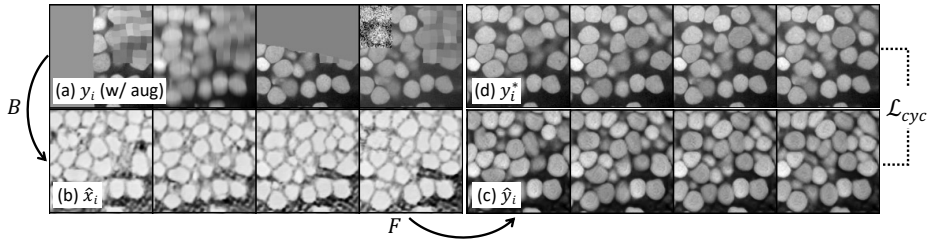


Fig. 3: Training augmentations. We show four consecutive slices of (a) augmented real I_Y input, (b) synthesized I_X volume, (c) reconstructed I_Y volume and (d) real I_Y volume w/o augmentations. By forcing the cycle consistency of (c) to (d), the model learns to restore corrupted regions with 3D context.

of all three representations to emphasize the correlation between them as the representations are calculated from the same instance masks. This also avoids using three independent discriminators that increase the system complexity. Those losses provided additional supervision in the absence of paired labels for I_Y .

Our method is connected to *semi-supervised* learning as we incorporate unlabeled images in optimization using losses without paired labels. We can also choose other semi-supervised objectives, *e.g.*, augmentation consistency [23]. Our work emphasizes the concept of leveraging unlabeled images in a unified translation-segmentation framework, while the specific design choices can vary.

2.3 Implementation

The full objective of CySGAN is the sum of losses in Sec. 2.1 and 2.2, which is

$$\begin{aligned}
 \mathcal{L} = & \underbrace{\mathcal{L}_{GAN}(F, D_Y^I) + \mathcal{L}_{GAN}(B, D_X^I) + \mathcal{L}_{cyc}(F, B)}_{\text{image-to-image translation}} + \underbrace{\mathcal{L}_{seg}(F) + \mathcal{L}_{seg}(B)}_{\text{supervised segm}} \\
 & + \underbrace{\mathcal{L}_{sc}(F, B) + \mathcal{L}_{GAN}(B, D_X^S) + \mathcal{L}_{GAN}(F, D_X^S)}_{\text{semi-supervised segm}}
 \end{aligned} \quad (6)$$

We assign a uniform weight for all losses without tweaking. We use a 3D U-Net [4] for F and B (they have identical architectures, but the parameters are not shared). We use 3D convolutional discriminators, where D_X and D_Y have a single input channel for the gray-scale images, while D_S has three input channels for the BCD representations. Following the CycleGAN [28] official code, we optimize the LSGAN [19] loss instead of the BCE GAN loss (Eqn. 2) for training stability. When calculating the segmentation losses, we detach the synthesized image to avoid the segmentation objectives affecting the image translation results.

U3D-BCD [16] uses multiple training augmentations like random missing, blurry and noisy regions (Fig. 3a). We keep them for better segmentation quality. However, enforcing the cycle consistency (Eqn. 3) using corrupted images can cause ambiguity in translation. Therefore we stream the training images

Table 1: **NucExM dataset.** We curated and densely annotated a *neuronal nuclei* segmentation dataset with two ExM volumes of zebrafish.

Sample	#Volumes	Volume Size (each)	Resolution (μm)	Ex. Ratio	#Instances
Zebrafish Brain	2	$2048 \times 2048 \times 255$	$0.325 \times 0.325 \times 2.5$	7.0	9.6K+8.8K

in both augmented and clean forms. As shown in Fig. 3 (each subfigure shows consecutive slices of a 3D volume), B transfers augmented y_i to \hat{x}_i , and F reconstructs \hat{x}_i to \hat{y}_i . Instead of calculating $\mathcal{L}_{cyc}(F, B)$ of \hat{y}_i to y_i , we enforce its similarity to the clean y_i^* (Fig. 3d). Our models keep the augmentations for better segmentation and additionally learn to restore corrupted regions using 3D context. Our implementation of the proposed CySGAN framework is based on the *PyTorch Connectomics* [15] open-source package.

3 Datasets

NucExM Dataset (Target). We curated the saturated nuclei segmentation annotation for two expansion microscopy (ExM) [3] volumes by two experts from a day 7 post-fertilization (dpf) zebrafish brain, imaged with confocal microscopy. These volumes have an anisotropic resolution of $0.325 \times 0.325 \times 2.5 \mu\text{m}$ in (x, y, z) order, with an approximate tissue expansion factor of 7.0. Thus the effective resolution becomes $0.046 \times 0.046 \times 0.357 \mu\text{m}$. The two volumes are of size $2048 \times 2048 \times 255$ voxels with 9.6K and 8.8K nuclei, respectively (Table 1).

Source Dataset and Resolution Matching. We use the NucMM-Z electron microscopy (EM) volume from the NucMM dataset [16] as the source (I_X and S_X in Fig. 1a). The original NucMM-Z covers nearly a whole zebrafish brain at a resolution of $0.48 \times 0.48 \times 0.48 \mu\text{m}$. Considering the different resolutions of two datasets, we crop a $200 \times 200 \times 255$ subvolume from NucMM-Z and upsample it to $512 \times 512 \times 255$, which contains 12K nuclei instances. During model training and inference, we downsample NucExM by $\times 4$ along x and y axes to $512 \times 512 \times 255$, so that both the resolution and size match for the two datasets.

Evaluation Metric. Following common practice in instance segmentation [6, 14], we choose average precision (AP) as the evaluation metric. Specifically, for our 3D volumetric data, we choose AP-50 (*i.e.*, AP with an IoU threshold of 0.5) and use the existing public implementation with improved efficiency [26].

4 Experiments

Methods in Comparison. We compare with Cellpose [24] and StarDist [27] pretrained models using their official implementation. For methods that conduct translation and segmentation sequentially, we test both histogram matching and CycleGAN [28] as translation models. We use U3D-BCD [16] for segmentation,

Table 2: **Benchmark results on the NucExM dataset.** We compare both pretrained segmentation networks and translation-segmentation models using the AP scores. In the two-step approaches, we use U3D-BCD [16] for segmentation. **Bold** and underlined numbers denote the 1st and 2nd results.

Method	Cellpose	StarDist	Histogram + Segm		CycleGAN + Segm		CySGAN (Ours)
			$I_X \rightarrow I_Y$	$I_Y \rightarrow I_X$	$I_X \rightarrow I_Y$	$I_Y \rightarrow I_X$	
AP-50 (V_1)	0.644	0.816	0.807	0.804	<u>0.867</u>	0.772	0.927
AP-50 (V_2)	0.765	0.875	0.826	0.816	<u>0.881</u>	0.777	0.934
Average	0.705	0.846	0.817	0.810	<u>0.874</u>	0.775	0.931

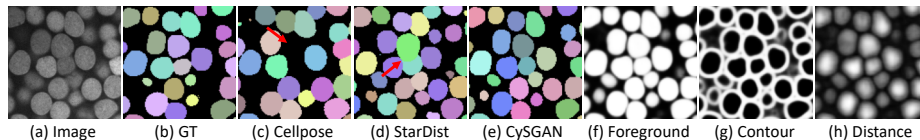


Fig. 4: Visual comparisons. (a) ExM image, (b) ground-truth instances, (c) Cellpose [24], (d) StarDist [27] and (e) CySGAN results. We also show (f-h) predicted segmentation representations of U3D-BCD used with CySGAN.

which is consistent with CySGAN generators but without the output channel for translated images. Specifically, we test the $I_X \rightarrow I_Y$ version that transfers I_X to I_Y , and trains a model in the target domain using synthesized images, and $I_Y \rightarrow I_X$ that transfers I_Y to I_X , and predicts the segmentation using a model trained in the source. For CycleGAN and CySGAN, we only use one ExM volume (V_1) to optimize the models and directly run inference on the other volume (V_2) that is not used for optimization.

Results. Table 2 shows that our CySGAN outperforms both pretrained models and the sequential translation-segmentation models with either histogram matching or CycleGAN for translation. Specifically, CySGAN outperforms the second-best model (CycleGAN+Segm, $I_X \rightarrow I_Y$) by absolutely 5.7%, demonstrating the effectiveness of our proposed framework. The visual results in Fig. 4 show that Cellpose segmentation has obvious false negatives, while StarDist masks do not align well with instance boundaries and overlap with each other. We empirically find that the strong star-convex shape prior often overlooks other features like boundaries. The results also show that $I_X \rightarrow I_Y$ versions generally perform better than $I_Y \rightarrow I_X$ ones in sequential models.

Ablation Studies. We further validate two important design choices of CySGAN, including the semi-supervised segmentation losses for the *unlabeled* domain (Eqn. 6) and data augmentations (Fig. 3). Table 3 shows that on the V_1 NucExM volume on which the models are optimized, removing either the training augmentations or the semi-supervised losses can result in obvious performance degradation of CySGAN, demonstrating the essentiality of those components.

Table 3: **Ablation study of CySGAN.** The results show the importance of data augmentations and semi-supervised segmentation losses in our CySGAN.

Configuration	CySGAN w/o Augment	CySGAN w/o Semi-sup	CySGAN (Ours)
AP-50 (V_1)	0.761 (-0.166)	0.878 (-0.049)	0.927

5 Conclusion

In this work, we present CySGAN, a unified translation-segmentation framework optimized with image translation losses as well as supervised and semi-supervised instance segmentation losses to tackle unlabeled domains. Important future directions include segmenting target domains where the instance structures are significantly different from those from the source domain.

Acknowledgement

This work has been partially supported by NSF awards IIS-1835231 and IIS-2124179 and NIH grant 5U54CA225088-03. Leander Lauenburg acknowledges the support from a fellowship within the IFI program of the German Academic Exchange Service (DAAD). Ignacio Arganda-Carreras acknowledges the support of the Beca Leonardo a Investigadores y Creadores Culturales 2020 de la Fundación BBVA. Edward S. Boyden acknowledges NIH 1R01EB024261, Lisa Yang, John Doerr, NIH 1R01MH123403, NIH 1R01MH123977, Schmidt Futures.

References

1. Caicedo, J.C., Goodman, A., Karhohs, K.W., Cimini, B.A., Ackerman, J., Haghghi, M., Heng, C., Becker, T., Doan, M., McQuin, C., et al.: Nucleus segmentation across imaging experiments: the 2018 data science bowl. *Nature methods* **16**(12), 1247–1253 (2019) [1](#)
2. Chartsias, A., Joyce, T., Dharmakumar, R., Tsaftaris, S.A.: Adversarial image synthesis for unpaired multi-modal cardiac data. In: *International workshop on simulation and synthesis in medical imaging*. pp. 3–13. Springer (2017) [3](#)
3. Chen, F., Tillberg, P.W., Boyden, E.S.: Expansion microscopy. *Science* **347**(6221), 543–548 (2015) [1](#), [7](#)
4. Çiçek, Ö., Abdulkadir, A., Lienkamp, S.S., Brox, T., Ronneberger, O.: 3d u-net: learning dense volumetric segmentation from sparse annotation. In: *MICCAI*. pp. 424–432. Springer (2016) [1](#), [2](#), [5](#), [6](#)
5. Cireşan, D., Giusti, A., Gambardella, L.M., Schmidhuber, J.: Deep neural networks segment neuronal membranes in electron microscopy images. In: *NeurIPS*. pp. 2843–2851 (2012) [3](#)
6. Cordts, M., Omran, M., Ramos, S., Rehfeld, T., Enzweiler, M., Benenson, R., Franke, U., Roth, S., Schiele, B.: The cityscapes dataset for semantic urban scene understanding. In: *Proceedings of the IEEE conference on computer vision and pattern recognition*. pp. 3213–3223 (2016) [7](#)

7. Cousty, J., Bertrand, G., Najman, L., Couprie, M.: Watershed cuts: Minimum spanning forests and the drop of water principle. *TPAMI* **31**, 1362–1374 (2008) [3](#)
8. Goodfellow, I., Pouget-Abadie, J., Mirza, M., Xu, B., Warde-Farley, D., Ozair, S., Courville, A., Bengio, Y.: Generative adversarial nets. *Advances in neural information processing systems* **27** (2014) [3](#)
9. Hoffman, J., Tzeng, E., Park, T., Zhu, J.Y., Isola, P., Saenko, K., Efros, A., Darrell, T.: Cycada: Cycle-consistent adversarial domain adaptation. In: *International conference on machine learning*. pp. 1989–1998. PMLR (2018) [3](#)
10. Huo, Y., Xu, Z., Bao, S., Assad, A., Abramson, R.G., Landman, B.A.: Adversarial synthesis learning enables segmentation without target modality ground truth. In: *2018 IEEE 15th international symposium on biomedical imaging (ISBI 2018)*. pp. 1217–1220. IEEE (2018) [3](#)
11. Isola, P., Zhu, J.Y., Zhou, T., Efros, A.A.: Image-to-image translation with conditional adversarial networks. In: *Proceedings of the IEEE conference on computer vision and pattern recognition*. pp. 1125–1134 (2017) [3](#)
12. Krasowski, N., Beier, T., Knott, G., Köthe, U., Hamprecht, F.A., Kreshuk, A.: Neuron segmentation with high-level biological priors. *TMI* **37**(4) (2017) [3](#)
13. Lee, K., Zung, J., Li, P., Jain, V., Seung, H.S.: Superhuman accuracy on the snemi3d connectomics challenge. *arXiv:1706.00120* (2017) [2](#), [3](#)
14. Lin, T.Y., Maire, M., Belongie, S., Hays, J., Perona, P., Ramanan, D., Dollár, P., Zitnick, C.L.: Microsoft coco: Common objects in context. In: *European conference on computer vision*. pp. 740–755. Springer (2014) [7](#)
15. Lin, Z., Wei, D., Lichtman, J., Pfister, H.: Pytorch connectomics: A scalable and flexible segmentation framework for em connectomics. *arXiv preprint arXiv:2112.05754* (2021) [7](#)
16. Lin, Z., Wei, D., Petkova, M.D., Wu, Y., Ahmed, Z., Zou, S., Wendt, N., Boulanger-Weill, J., Wang, X., Dhanyasi, N., et al.: Nucmm dataset: 3d neuronal nuclei instance segmentation at sub-cubic millimeter scale. In: *International Conference on Medical Image Computing and Computer-Assisted Intervention*. pp. 164–174. Springer (2021) [1](#), [2](#), [3](#), [5](#), [6](#), [7](#), [8](#)
17. Liu, F.: Susan: segment unannotated image structure using adversarial network. *Magnetic resonance in medicine* **81**(5), 3330–3345 (2019) [2](#), [3](#)
18. Liu, M.Y., Breuel, T., Kautz, J.: Unsupervised image-to-image translation networks. *Advances in neural information processing systems* **30** (2017) [3](#)
19. Mao, X., Li, Q., Xie, H., Lau, R.Y., Wang, Z., Paul Smolley, S.: Least squares generative adversarial networks. In: *Proceedings of the IEEE international conference on computer vision*. pp. 2794–2802 (2017) [6](#)
20. Pang, Y., Lin, J., Qin, T., Chen, Z.: Image-to-image translation: Methods and applications. *IEEE Transactions on Multimedia* (2021) [3](#)
21. Rivron, N.C., Frias-Aldeguer, J., Vrij, E.J., Boisset, J.C., Korving, J., Vivié, J., Truckenmüller, R.K., Van Oudenaarden, A., Van Blitterswijk, C.A., Geijsen, N.: Blastocyst-like structures generated solely from stem cells. *Nature* **557**(7703), 106–111 (2018) [1](#)
22. Ronneberger, O., Fischer, P., Brox, T.: U-net: Convolutional networks for biomedical image segmentation. In: *MICCAI*. pp. 234–241. Springer (2015) [1](#), [3](#)
23. Sohn, K., Berthelot, D., Carlini, N., Zhang, Z., Zhang, H., Raffel, C.A., Cubuk, E.D., Kurakin, A., Li, C.L.: Fixmatch: Simplifying semi-supervised learning with consistency and confidence. *Advances in Neural Information Processing Systems* **33**, 596–608 (2020) [6](#)

24. Stringer, C., Wang, T., Michaelos, M., Pachitariu, M.: Cellpose: a generalist algorithm for cellular segmentation. *Nature Methods* **18**(1), 100–106 (2021) [1](#), [2](#), [3](#), [5](#), [7](#), [8](#)
25. Turaga, S.C., Briggman, K.L., Helmstaedter, M., Denk, W., Seung, H.S.: Maximin affinity learning of image segmentation. In: *NeurIPS*. pp. 1865–1873 (2009) [3](#)
26. Wei, D., Lin, Z., Franco-Barranco, D., Wendt, N., et al.: Mitoem dataset: Large-scale 3d mitochondria instance segmentation from em images. In: *International Conference on Medical Image Computing and Computer-Assisted Intervention*. pp. 66–76. Springer (2020) [3](#), [5](#), [7](#)
27. Weigert, M., Schmidt, U., Haase, R., Sugawara, K., Myers, G.: Star-convex polyhedra for 3d object detection and segmentation in microscopy. In: *Proceedings of the IEEE/CVF Winter Conference on Applications of Computer Vision*. pp. 3666–3673 (2020) [1](#), [2](#), [3](#), [5](#), [7](#), [8](#)
28. Zhu, J.Y., Park, T., Isola, P., Efros, A.A.: Unpaired image-to-image translation using cycle-consistent adversarial networks. In: *Proceedings of the IEEE international conference on computer vision*. pp. 2223–2232 (2017) [2](#), [3](#), [4](#), [6](#), [7](#)
29. Zlateski, A., Seung, H.S.: Image segmentation by size-dependent single linkage clustering of a watershed basin graph. *arXiv:1505.00249* (2015) [3](#)

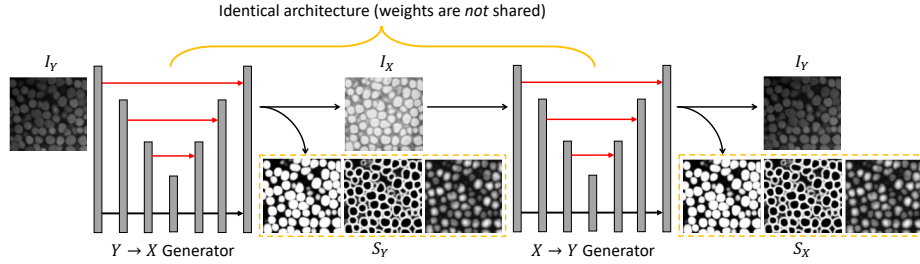


Fig. A-1: Architecture details of CySGAN. Given an image sampled from I_Y , the *backward* generator predicts both the transferred image in I_X and the segmentation representations. Then the *forward* generator takes only the translated image as input and predicts both the reconstructed image and segmentation representations. The two generators have exactly the same architecture, but the weights are *not* shared as they translate images in different domains.

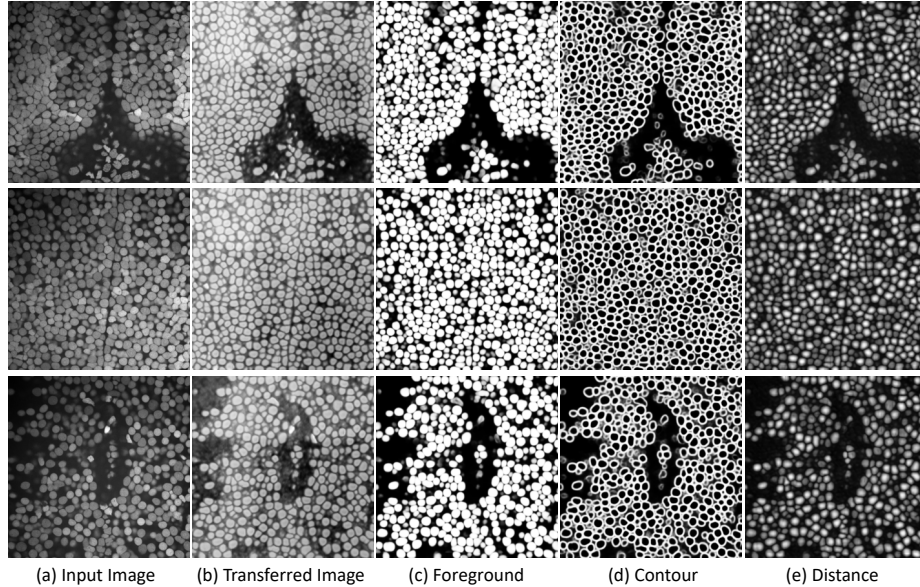


Fig. A-2: Qualitative results of CySGAN. We show multiple slices of (a) input NucExM images, as well as (b) transferred images, (c) predicted binary foreground masks (B), (d) predicted instance contour maps (C) and (e) predicted distance transform maps (D) of our proposed CySGAN model.

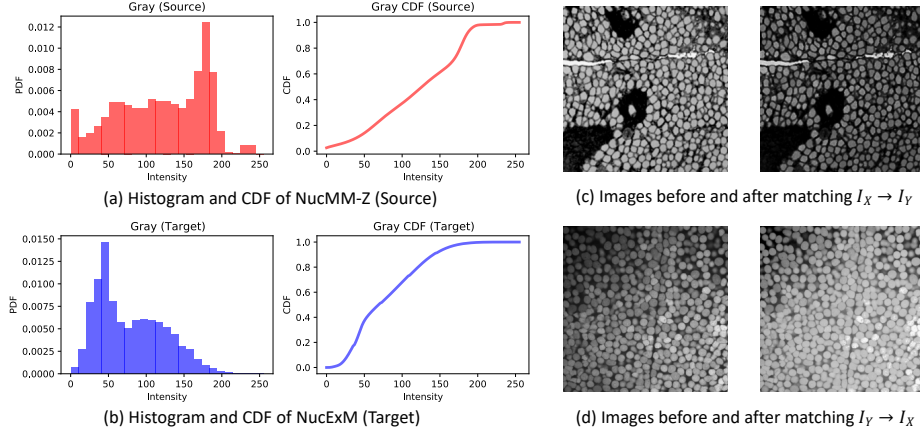


Fig. A-3: Histogram matching between EM and ExM images. We show the histograms and cumulative distribution functions (CDFs) of (a) electron microscopy (EM) and (b) expansion microscopy (ExM) images. The effect of histogram matching is shown in (c) and (d) for both matching directions.

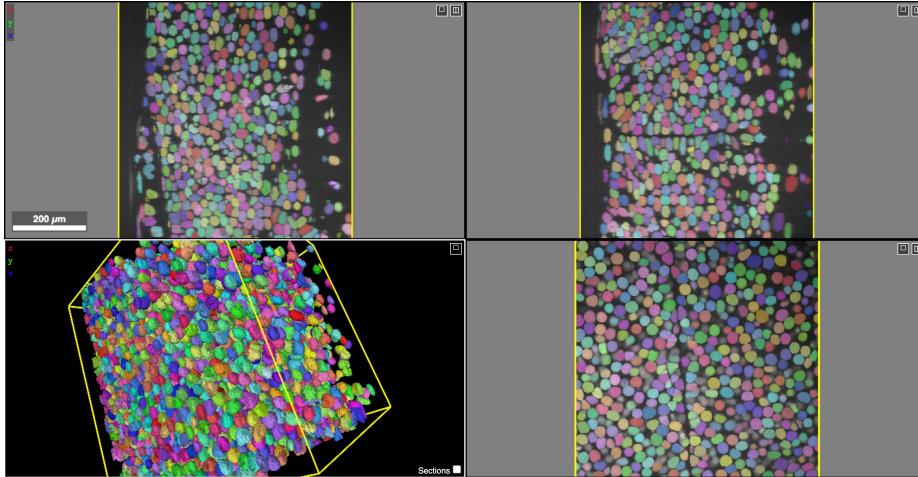


Fig. A-4: Multi-view visualization and 3D meshes of NucExM. We show the composite views of microscopy images and instance masks of V_1 in the NucExM dataset, as well as the 3D meshes of nuclei. We generated the visualizations using the Neuroglancer (<https://github.com/google/neuroglancer>).